# Shear Design of Reinforced Concrete Elements with Steel Fibers

**Díaz Fondevila Alejandra, Almenar Martín\***

Institute of Structures, National University of Tucumán, Argentina.
Corresponding author. Email address: malmenar@herrera.unt.edu.ar

**Abstract:** Experimental research shows that the addition of ductile fibers improves the tensile strength, ductility and concrete's energy absorption capacity. As a consequence of the improvement of the post-cracking behavior, the addition of dispersed ductile fibers can increase the ductility, the shear resistance and the toughness of reinforced concrete beams, changing the type of failure from brittle to ductile. Many studies have considered the possibility of using steel fibers to partially resist shear and thus decrease shear reinforcement. This concept has even been adopted by some design codes such as ACI-318 or the Fib Model Code 2010 and has great potential for application in critical points of reinforced concrete structures where it is difficult to arrange shear reinforcement, such as beam - column joints. Despite this, fiber-reinforced concrete is still rarely used in load - bearing elements. In this work, it is proposed to numerically study the behavior of fiber-reinforced concrete beams tested at shear by other researchers in order to evaluate the contribution of steel fibers to the mechanism of resistance to shear.

**Key words:** fiber-reinforced concrete; steel fibers; shear design

## 1. Introduction

The appearance of cracks in concrete was long considered dangerous and delayed the use of reinforced concrete (RC). It is now known that hairline cracks remain as such if the reinforcing bars are well distributed and not too large diameters are used. This avoids large cracks and the danger of corrosion (Möller, 2007)[1].

As is well known, adding fibers to concrete can control crack propagation by increasing residual strength and toughness. When incorporated into reinforced concrete components, fibers contribute to shear strength, allowing for at least a partial reduction in conventional reinforcement and improving the adhesion between steel and concrete, potentially reducing the length of adhesion. But an important point is that fibers can control the width of cracks, which means they have significant advantages in extending the service life and durability of the structure (Fasciolo et al., 2018)[2]. Except in special circumstances, the presence of fibers will not cause significant changes in the hardened material before the first cracking of the matrix. The main reason for adding fibers is to provide post-cracking transfer ability (Zerbino et al., 2020)[3].

Although Fiber Reinforced Concrete (FRC) has an academic history of more than 50 years, its adoption in practice has been mainly limited to non-critical elements. For concrete to be used on a regular basis, a rational framework of the material's models that identifies its key parameters must be established (Amin, 2015)[4]. There are two main reasons why

HRF is underutilized, one theoretical and the other technological. The first one forces designers to consider fracture mechanics concepts to describe the post-cracking residual strength due to the crack stitching effect provided by the fibers. The second reason is mainly due to aspects related to workability. If the correct admixtures are not used, filling with HRF can be extremely complicated (di Prisco, et al., 2013)[5].

One of the major advances in recent years has been the development of structural design standards and their incorporation into regulations, with the most important being the FIB Model Code or FIB Model Code 2010 (2012)[6]. This document not only adopts a standard for applying the concept of residual strength to HRF characterization, but also proposes recommendations for HRF classification based on this standard. Therefore, it is possible today to design structures using a type of HRF and evaluate alternative solutions for fiber type and content to comply with the sought response (Zerbino et al., 2020)[3].

One area where it is considered that steel fibers can contribute is in the area of shear strength either as a full or partial replacement in combination with conventional shear reinforcement (Amin, 2015)[4]. In examining research on the shear behavior and strength of HRF beams, most studies have focused on members containing only fibers as reinforcement, with few studies evaluating the combined capacity of fibers with conventional shear reinforcement (Amin & Foster, 2016)[7].

The general objective of this work is to contribute to the efficient shear design of reinforced concrete structural elements reinforced with steel fibers. It is proposed to numerically study the behavior of reinforced concrete beams with fibers tested in shear by other researchers in order to evaluate the contribution of the fibers in the shear strength.

The following partial objectives are proposed:

- Numerically obtain and analyze the response of fiber-reinforced concrete at the material level by simulating standardized shear tests available in the literature.
- To numerically obtain and analyze the shear response of fiber reinforced concrete beams tested by other researchers.

In this work, the numerical simulations were performed using the Ansys Workbench program, using a numerical model available in its library suitable for representing the behavior of the HRF.

## 2. Constitutive Model Used

An elastoplastic model was used to reproduce the behavior of concrete. In this model, the relationship between the stress tensor σ, the strain tensor ε and the plastic strain tensor $\varepsilon^{pl}$ is given by

$$\boldsymbol{\sigma} = \boldsymbol{C}\left(\boldsymbol{\varepsilon} - \boldsymbol{\varepsilon^{pl}}\right) \tag{1}$$

Where, $C$ is the fourth order elastic constitutive tensor for a linear and isotropic elastic material. Such tensor is determined by means of the elastic parameters $E$ and μ which are Young's modulus and Poisson's coefficient respectively. The increase of the plastic deformations is calculated by the following flow rule

$$\dot{\boldsymbol{\varepsilon}}^{\boldsymbol{pl}} = \dot{\lambda}\,\frac{\partial Q_{MW}}{\partial \boldsymbol{\sigma}} \tag{2}$$

where $Q_{MW}$ is a potential function to be defined later and $\dot{\lambda}$ is the increment of the plastic multiplier. The plastic multiplier can be determined by means of the loading and unloading confections defined below

$$f_{MW} \leq 0, \quad \dot{\lambda} \geq 0, \quad f_{MW}\,\dot{\lambda} = 0, \tag{3}$$

Where $f_{MW}$ is the creep function. This model uses the creep function of Menetrey and Willam (1995)[8], which is schematized in Fig. 1. Within this surface, the material exhibits isotropic linear elastic behavior. Upon reaching this surface, the material begins to experience plastic deformations, which are determined by the previously defined expressions.
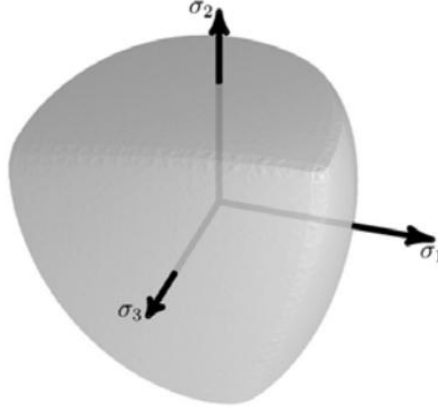
**Figure 1.** Menetry-Willam yield surface.

The creep function is defined as

$$f_{MW} = \frac{c_2}{c_3}\left[\sqrt{\frac{2}{3}}I_1 + r\sqrt{2J_2}\right] + 2J_2 - \frac{1}{c_3},$$

(4)

where, $I_1$ is the first invariant of $\sigma$ and $J_2$ the second invariant of the stress deviatoric tensor $S$. In equation (4), $c_2$, $c_3$ and $r$ depend on material parameters and hardening-softening functions:

$$c_2 = \frac{1}{\sqrt{6}}\left[\frac{1}{\overline{R_c}} - \frac{1}{\overline{R_b}} + \frac{\overline{R_b}-\overline{R_t}}{\overline{R_c}^2}\right],$$

(5)

$$c_3 = \frac{3}{2}\frac{1}{\overline{R_c}^2}$$

(6)

$$r = \frac{4(1-e^2)cos^2\theta+(2e-1)^2}{2(1-e^2)\cos\theta+(2e-1)\sqrt{4(1-e^2)cos^2\theta+5e^2-4e}}$$

(7)

$$\overline{R_t} = R_t\Omega_{tc} \ , \ \ \overline{R_c} = R_c\Omega_c \ , \ \ \overline{R_b} = R_b\Omega_c,$$

(8)

$$\Omega_{tc} = \begin{cases} \Omega_t & \kappa_c \leq \kappa_{cm} \\ \Omega_t\Omega_c & \kappa_c > \kappa_{cm} \end{cases},$$

(9)

$$\epsilon = \frac{\overline{R_t}}{\overline{R_b}} * \frac{\overline{R_b}^2-\overline{R_c}^2}{\overline{R_c}^2-\overline{R_t}^2} \ , \ \ e = \frac{1+\epsilon}{2-\epsilon},$$

(10)

$$\cos 3\theta = \frac{3\sqrt{3}}{2}\frac{J_3}{\sqrt{J_2^3}},$$

(11)

where: $R_t$, $R_c$ and $R_b$ are the tensile, compressive and biaxial strengths, respectively. $\Omega_t$ and $\Omega_c$, are the stiffening-softening functions, which depend on $K_t$ and $K_c$ which are the tensile and compressive stiffening variable respectively. $J_3$ is the third invariant of the stress deviatoric tensor $S$, and $K_{cm}$ is a material parameter which is a threshold in the $\Omega_c$ function and will be detailed later.

The increment of the hardening variables can be calculated as:

$$\dot{\kappa}_c = \frac{\alpha_c}{R_t}\sigma \cdot \dot{\varepsilon}^{pl},$$

(12)

$$\dot{\kappa}_t = \frac{\alpha_t}{R_t}\sigma \cdot \dot{\varepsilon}^{pl},$$

(13)

where, $\sigma \cdot \varepsilon^{pl}$ denotes the scalar product between the stress tensor and the increment of the plastic deformation tensor respectively. $\alpha_c$ and $\alpha_t$ are the compressive and tensile weight functions respectively defined as:

3

$$\alpha_c = 1 - \alpha_t, \tag{14}$$

$$\alpha_t = \begin{cases} 0 & \tan\alpha < -2 \\ \frac{1}{1+e^{-10\tan\alpha}} & -2 \le \tan\alpha \le 2 \\ 1 & \tan\alpha > -2 \end{cases} \tag{15}$$

$$\tan\alpha = \frac{I_1}{\sqrt{J_2}}. \tag{16}$$

The compression hardening-softening function is defined as:

$$\Omega_c = \Omega_{ci} + (1 - \Omega_{ci})\sqrt{2\frac{\kappa_c}{\kappa_{cm}} - \frac{\kappa_c^2}{\kappa_{cm}^2}}, \text{ para } \kappa_c < \kappa_{cm}, \tag{17}$$

$$\Omega_c = 1 - (1 - \Omega_{cu})\left(\frac{K - K_{cm}}{K_{cu} - K_{cm}}\right)^2, \text{ para } \kappa_{cm} < \kappa_c < \kappa_{cu}, \tag{18}$$

$$\Omega_c = \Omega_{cr} + (\Omega_{cu} - \Omega_{cu})e^{\left(2\frac{\Omega_{cu}-1}{K_{cu}-K_{cm}} * \frac{\kappa_c - K_{cu}}{\Omega_{cu}-\Omega_{cr}}\right)}, \text{ para } \kappa_c > \kappa_{cu}, \tag{19}$$

where $k_{cm}$ and $k_{cu}$ are material parameters that correspond to the variable value of hardening in compression at the transition of its different branches. In particular, $k_{cm}$ is the value of the compression hardening variable at the peak of the function $\Omega_c$ and occurs when $\Omega_c = 1$. $\Omega_{ci}$ is the initial value of $\Omega_c$, $\Omega_{cu}$ is the value corresponding to $K_{cu}$, and $\Omega_{cr}$ is the value when $K_c$ tends to infinity.

The tensile hardening-softening function is defined as:

$$\Omega_t = e^{-\frac{\kappa_c}{a_t}}, \tag{20}$$

$$a_t = \frac{g_{ft}}{R_t}, \tag{21}$$

$$g_{ft} = max\left(\frac{G_{ft}}{L_i}, \frac{R_t^2}{E}\right), \tag{22}$$

where $g_{ft}$ is the tensile fracture energy. $L_i$ is the effective length of the element and must be determined in such a way that the following equation is satisfied

$$\int_0^\infty \Omega_t \, d\kappa_t = \frac{g_{ft}}{R_t}. \tag{23}$$

The hardening-softening functions in tension and compression can be seen in Fig. 2. These functions can be obtained experimentally by uniaxial tension and compression tests.
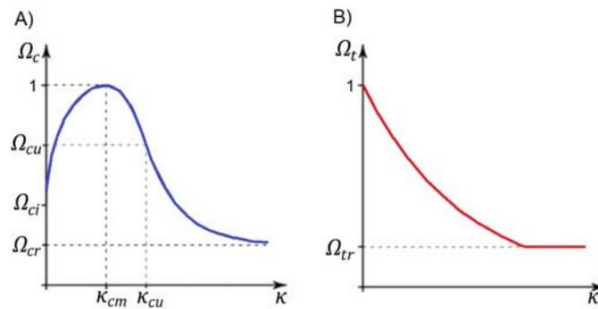


**Figure 2.** Hardening-softening functions in (A) tension and (B) compression.

The model uses non-associative flow, so the potential function is defined as:

$$Q_{MW} = 2J_2 + B_g\sqrt{2J_2} + C_g\frac{1}{\sqrt{3}}I_1, \tag{24}$$

$$B_g = \frac{2\overline{R_c}\tan\Psi - \sqrt{2R_t}}{\sqrt{3}(1 - \sqrt{2}\tan\Psi)}, \tag{25}$$

$$C_g = \frac{B_g}{\sqrt{2}} + \frac{2\overline{R_t}}{\sqrt{3}}. \qquad\qquad (26)$$

Where $\Psi$ is the angle of dilatance.

To summarize, the model has 3 sets of parameters to be defined:

- Elastic Parameters: $E$ and $\mu$.
- Creep Surface and Potential Function Parameters: $R_t$, $R_c$, $R_b$ and $\Psi$.
- Parameters of the hardening-softening functions: $K_{cm}$, $K_{cu}$, $\Omega_{ci}$, $\Omega_{cu}$, $\Omega_{cr}$, $\Omega_{tr}$ and $\Omega_{ft}$.

## 3. FIP Shear Test Simulation

Although previous experiments carried out by Frediani, et al. (2019)[9] applying the Menetrey - Williams model demonstrate that it is able to satisfactorily reproduce the behavior of HRF in bending. In order to achieve the objectives of this work, it is necessary to verify the performance of such model in the event of material failure by shear. This evaluation is performed by numerical reproduction of the standardized shear test conducted by the FIP (Federation Internationale de la Precontrainte) in order to compare the numerical response with experimental results available in the literature.

From the experimental studies carried out by Khanlou, et al. (2013)[10], information on the shear response in concrete blocks is obtained, which is useful for the calibration of parameters included in the numerical model. In the standard FIP test, the specimen is theoretically subjected to pure shear forces by means of two parallel planes, and the occurrence of bending moments is minimized due to the eccentricity of such actions. In general, this test is used because of the ease construction of specimens whose dimensions correspond to $250 \times 250 \times 450$ mm. Figure 3 shows the scheme of loads and supports proposed to simulate the test.
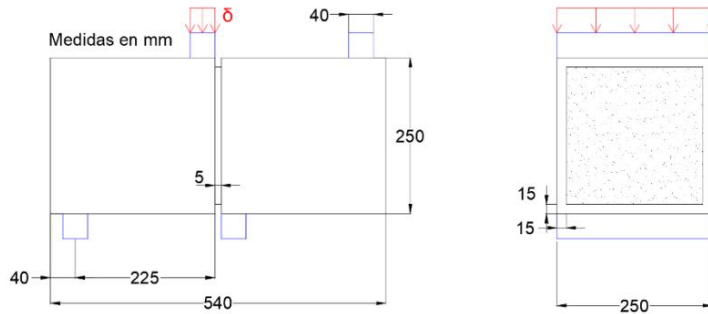


**Figure 3.** Schematic of the FIP assay.

To ensure that the failure plane is determined and to avoid cracks outside of it, a 15 mm deep notch is cut around the entire block to be tested. The area resisting the applied stress is then $220 \times 220$ mm as shown in Figure 4.



**Figure 4.** Test tube used in the test conducted by Khanlou, et al. 2013[10].

The compositions of the mixtures proposed in the work of Khanlou, et al. 2013[10] are presented according to Table 1.

**Table 1.** Composition of mixtures used by Khanlou, et al. 2013 [10]

| Mix | Fiber Dose (kg/m³) | Volume of Fibers (%) | Cement (kg/m³) | Water (kg/m³) | A/c | Coarse aggregate (kg/m³) | Sand (kg/m³) |
|------|------|------|------|------|------|------|------|
| C-35-20 | 20 | 0.25 | 287 | 172 | 0.6 | 1040 | 906 |
| C-35-40 | 40 | 0.51 | 292 | 175 | 0.6 | 920 | 1007 |
| C-35-60 | 60 | 0.76 | 308 | 185 | 0.6 | 750 | 1129 |
| C-35-80 | 80 | 1 | 317 | 190 | 0.6 | 600 | 1252 |

The fiber dosages were 20, 40, 60 and 80 kg/m³, high strength, hooked at the ends, cold drawn. The dimensions and properties of the fibers are shown in Table 2.

**Table 2.** Properties of the fibers used by used by Khanlou, et al. 2013 [10]

| Long $l_f$ (mm) | Diameter $d_f$ (mm) | Appearance $l_f/d_f$ | Tensile strength (MPa) | Form |
|------|------|------|------|------|
| 60 | 0.75 | 80 | 1050 | ‾\_⌐‾\_‾ |

In the representation by means of the computational model, after creating the geometry, the mesh to be used and the size of the elements that compose it are defined. All of them are solid elements of quadratic order defined by a hexahedron with 20 nodes and a tetrahedron with 10 nodes, with each node having 3 degrees of displacement freedom. Figure 5 shows the mesh used in the numerical model, as well as the points where the relative vertical displacements were measured for comparison with the experimental data. The mesh used has 4,832 elements and 12,690 nodes of variable size, with greater refinement in the zone where the shear failure occurs.
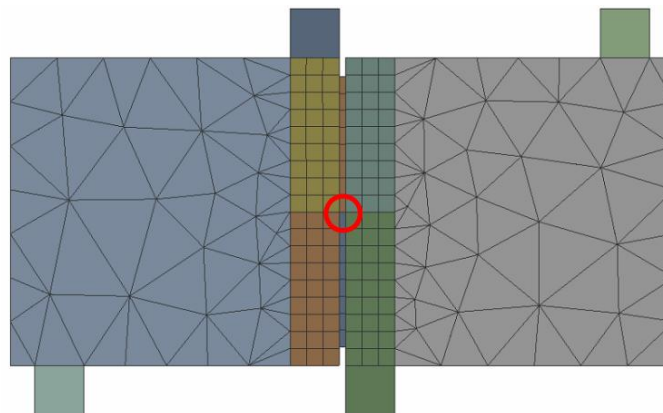


**Figure 5.** FE mesh used for numerical tests.

Next, the calibration of the models is performed based on the adjustment from the experimental response of simple concrete, i.e. without fibers and for doses of 20, 40, 60, 80 kg/m³ of fibers. Figure 6 contrasts the numerical results ("A") with the experimental ones ("E"), in terms of shear stress vs vertical displacement. For the case of plain concrete in the experimental test, the curves are only recorded up to the peak load, then it drops and no values are obtained. Accordingly, the numerical model is also unable to capture the abrupt change that corresponds to a sudden brittle failure for a small shear deformation. The parameters used in the numerical models can be seen in Table 3.
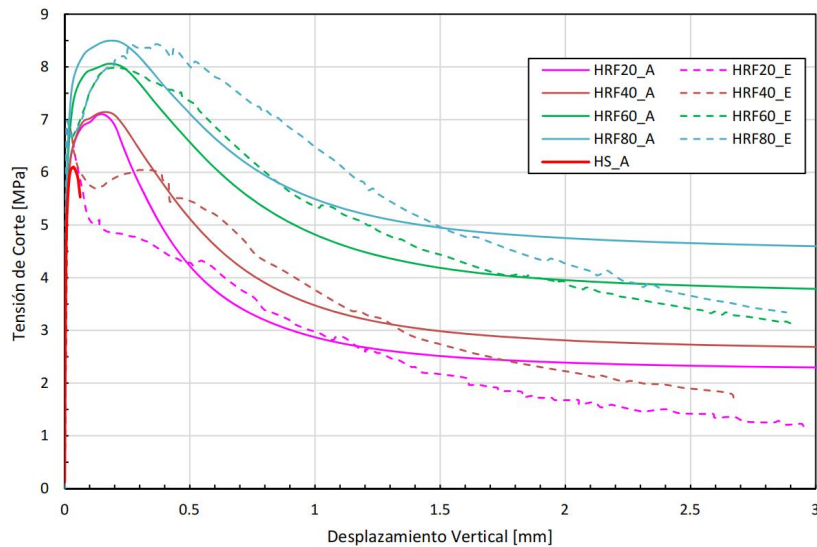
**Figure 6.** Numerical adjustment: shear stress vs. vertical displacement.

**Table 3.** Parameters used in the numerical reproduction of the FIP test

| Parameter | H. Simple | 20 kg/m$^3$ | 40 kg/m$^3$ | 60 kg/m$^3$ | 80 kg/m$^3$ |
|---|---|---|---|---|---|
| $E$ (MPa) | 28,000 | 28,000 | 28,000 | 28,000 | 28,000 |
| μ | 0.2 | 0.2 | 0.2 | 0.2 | 0.2 |
| $R_c$ (MPa) | 35 | 35 | 35 | 35 | 35 |
| $R_t$ (MPa) | 3.5 | 3.5 | 3.5 | 4.1 | 4.4 |
| $R_b$ (MPa) | 42 | 42 | 42 | 42 | 42 |
| Ψ | 13 | 13 | 13 | 13 | 13 |
| $K_{cu}$ | 0.001 | 0.001 | 0.001 | 0.001 | 0.001 |
| $K_{cu}$ | 0.004 | 0.025 | 0.03 | 0.045 | 0.05 |
| $\Omega_{ci}$ | 0.75 | 0.75 | 0.75 | 0.75 | 0.75 |
| $\Omega_{cu}$ | 0.9 | 0.9 | 0.9 | 0.9 | 0.9 |
| $\Omega_{cr}$ | 0.05 | 0.27 | 0.3 | 0.38 | 0.45 |
| $G_{ft}$ (N/m) | 80 | 400 | 600 | 1,000 | 1,200 |
| $\Omega_{tr}$ | 0.05 | 0.05 | 0.1 | 0.17 | 0.2 |

Figure 7 shows an equivalent plastic deformation map at failure for one of the tests. Such failure occurs suddenly throughout the section once compressive stresses are reached at the top of the notch, leading to failure of the material.
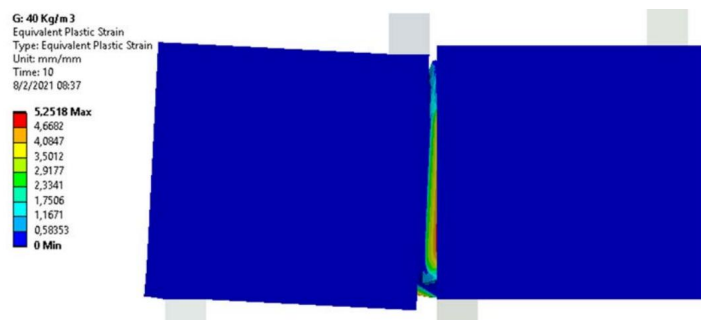


**Figure 7.** Equivalent plastic deformation map. HRF 40. Deformation ×3.

## 4. Simulation of Fiber-Reinforced Reinforced Concrete Beams

Although the previous section shows that the model used is capable of satisfactorily reproducing the behavior of the HRF under shear failure, the objective of this section is to verify the model in a slightly more complex structure, widely used in practice, such as reinforced concrete beams whose proposed configuration leads to shear failure. Also, in these numerical tests, it is intended to evaluate the influence of the different parameters on the response given by the model. The experimental tests to be reproduced are found in the thesis of Amin, (2015)[4], who tested different variants of reinforced concrete beams with and without fibers.

With the main objective of knowing the shear behavior of HRF in combination with traditional reinforcement reinforcement, Amin (2015)[4] carried out a large-scale beam test whose dimensions were 700 × 300 × 5000 mm. The evaluation proposals include concrete beams with longitudinal reinforcement, to which are added: stirrups, steel fibers, and finally, the combination of both. The test geometry is shown in Figure 8.
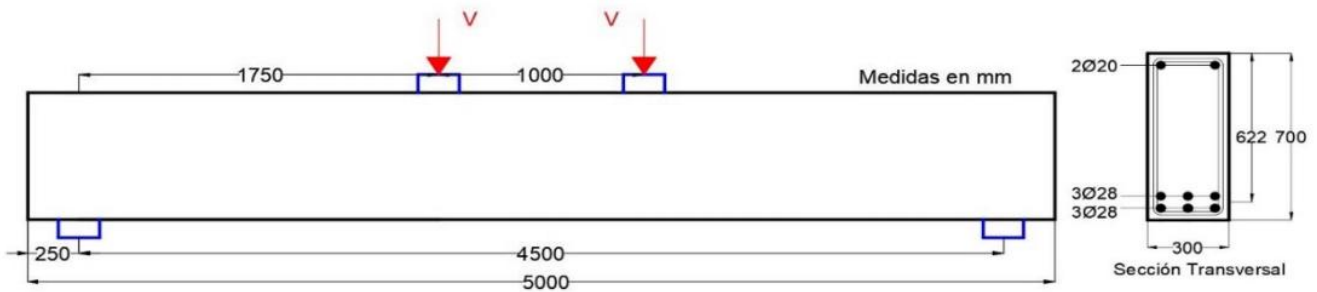


**Figure 8.** Geometry and configuration of loads used by Amin, (2015)[4].

The authors set the ratio between the shear length and the effective height of the beam (Lc/d) as 2.8 to avoid any arching effect, delimiting the constant moment zone at 1,000 mm and the constant shear zone at 1,750 mm. In the latter, the transverse reinforcement is located, see Figure 9, with a spacing of 450 mm that responds to the minimum proposed by the Eurocode. The stirrups are divided into two branches, diameters 6 and 10 mm with yield stresses of 550 and 450 MPa respectively. Likewise, the movement proposes sufficient longitudinal reinforcement so that the failure mechanism of the beam does not develop by bending, providing 6Φ28 in the lower fibers and 2Φ20 in the upper fibers with yield stresses of 550 MPa.
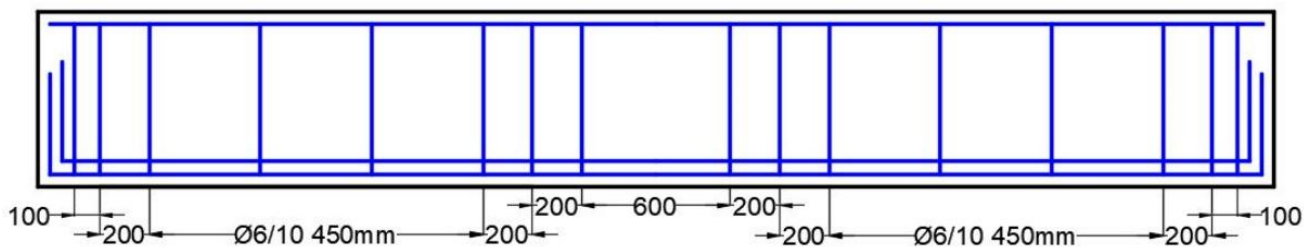


**Figure 9.** Reinforcement arrangement used by Amin, (2015)[4].

The mixtures tested in the laboratory yield a compressive strength f'c = 32MPa and modulus of elasticity E = 28000MPa. Two doses of fibers are used in the mixtures, 25 kg/m$^3$ and 50 kg/m$^3$. These are structural steel fibers, 0.9 mm in diameter and 60 mm in length with a tensile strength of 2,300 MPa and double hooks at the ends to increase anchorage in the concrete matrix.

The following configurations are numerically simulated:

- Concrete beams without fibers and without transverse reinforcement.
- Concrete beams with fibers and without transverse reinforcement.
- Beams with a combination of fibers and transverse reinforcement.

It should be clarified that not all cases to be simulated have the experimental curves, so some numerical curves are obtained from extrapolations of the model. In this way, the contribution of each component to the shear resistance (contribution of plain concrete, fibers and stirrups) can be individualized.

Solid quadratic and bar finite elements are used, with their union specified by the coincidence of nodes between both elements to ensure compatibility in displacements. The concrete mesh uses solid elements defined by 20-node hexahedra, while 3-node bar elements are used for the reinforcement. The mesh used has 9,520 elements and 44,293 nodes. Figures 10 and 11 show the finite element meshes adopted in the numerical simulation. It should be clarified that in the beams without transverse reinforcement or with only one stirrup, the elements that do not correspond to the model to be carried out are suppressed. Additionally, it should be clarified that in Figure 10, only two stirrups are represented in correspondence with the maximum number of stirrups that collaborated to resist the shear reported in the experimental work.
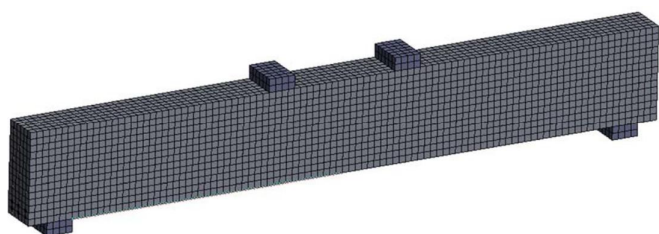


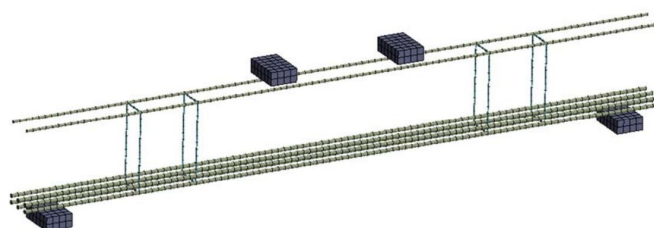**Figure 10.** Finite element mesh for concrete.



**Figure 11.** Finite element mesh for reinforcement.

The responses of the HARF beams are obtained using the Ansys Workbench program. In the model, the adjusted parameters are introduced from the data provided by (Amin, 2015)[4]. Table 4 indicates the adopted parameters.

**Table 4.** Parameters used in the numerical simulation of beams

| Parameter | H. Simple | 25kg/m³ of fibers | 50 kg/m³ of fibers |
|---|---|---|---|
| $E$ (MPa) | 28,000 | 28,000 | 28,000 |
| μ | 0.2 | 0.2 | 0.2 |
| $R_c$ (MPa) | 32 | 32 | 32 |
| $R_t$ (MPa) | 1.4 | 1.4 | 1.4 |
| $R_b$ (MPa) | 39.44 | 39.44 | 39.44 |
| $\Psi$ (o) | 6 | 6 | 6 |
| $K_{cu}$ | 0.0006 | 0.0006 | 0.0006 |
| $K_{cu}$ | 0.005 | 0.025 | 0.04 |
| $\Omega_{ci}$ | 0.4 | 0.4 | 0.4 |
| $\Omega_{cu}$ | 0.65 | 0.65 | 0.65 |
| $\Omega_{cr}$ | 0.65 | 0.25 | 0.33 |
| $G_{ft}$ (N/m) | 20 | 100 | 750 |
| $\Omega_{tr}$ | 0.05 | 0.25 | 0.33 |

The numerical responses (A) are presented in Figures 12, 13, 14, 15, 16 and 17, in which the load curves are plotted as a function of the deflection measured at the center span on the bottom face of the beams and compared with the curves corresponding to the experimental results (E). The curves are given as Beam W-X, where W is the fiber content in kg/m$^3$ and X is the diameter of the stirrup. All figures include the experimental results for the beam without fibers and without stirrups as a control. Figures 12, 13, 14, 15, 16 and 17 show that the numerical simulations correctly capture the behavior of the beams.
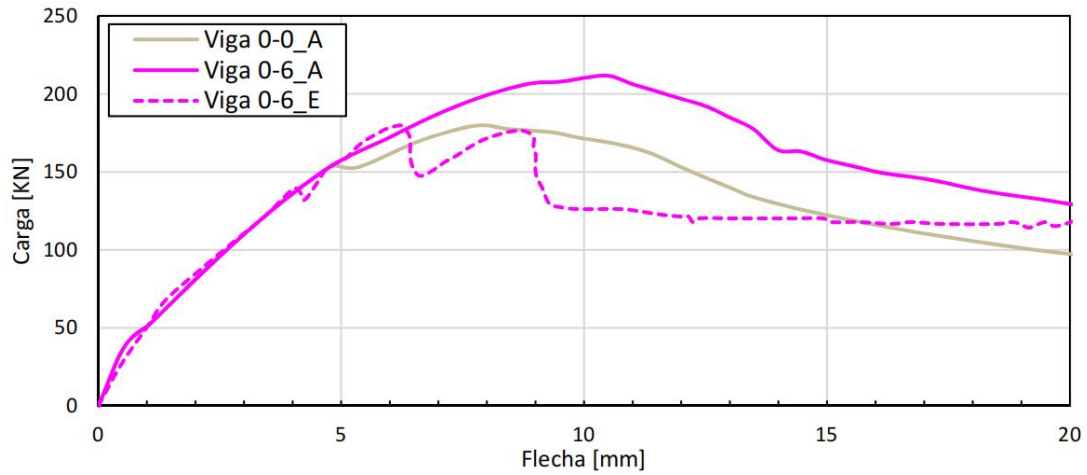
**Figure 12.** Load vs deflection curve for concrete without fibers. Stirrups Φ6.
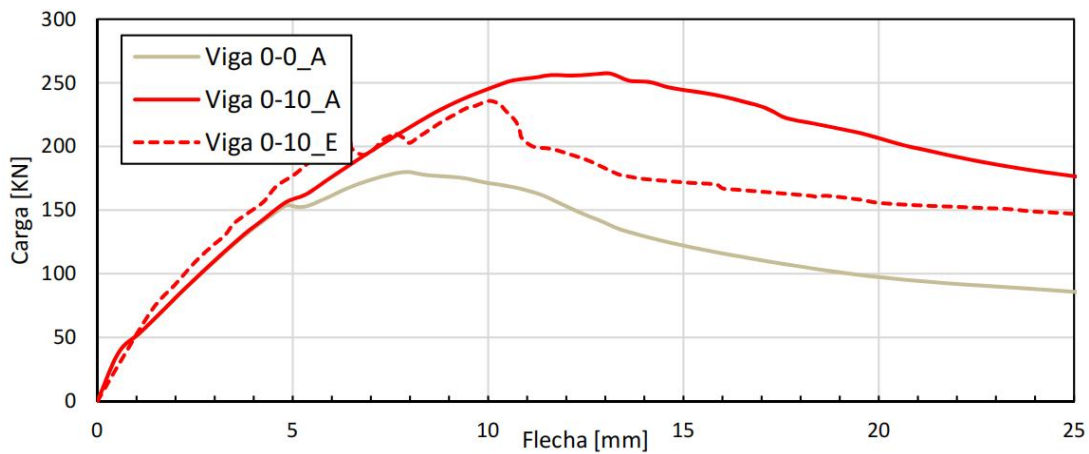
**Figure 13.** Load vs deflection curve for concrete without fibers. Stirrups Φ10.

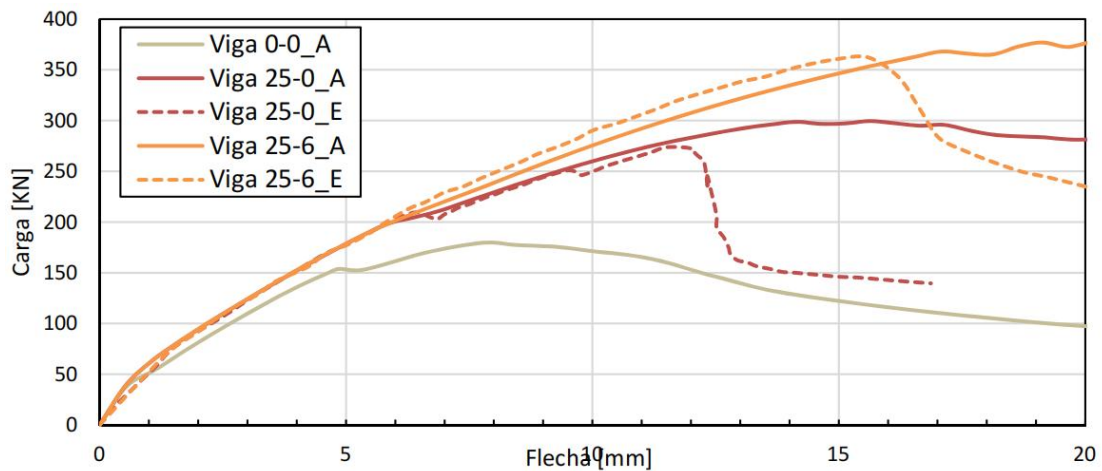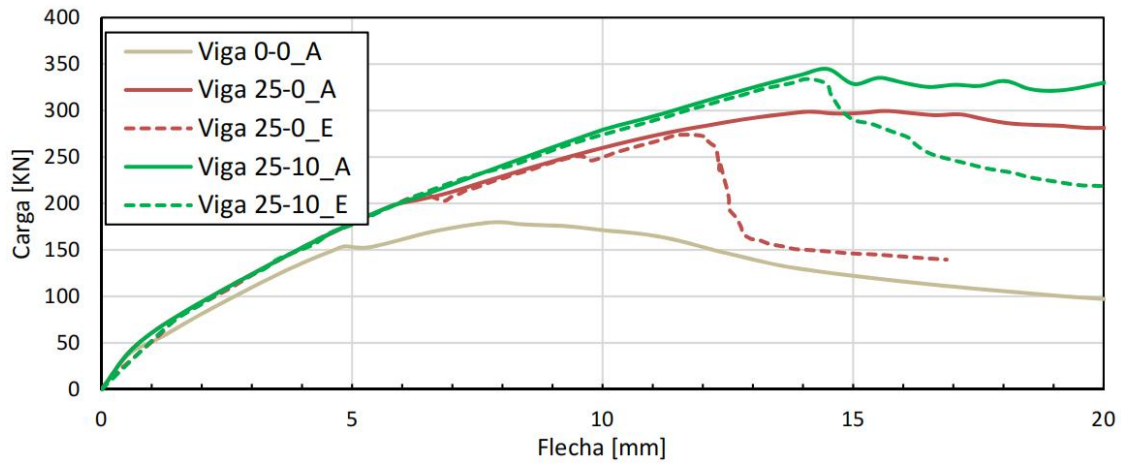**Figure 14.** Load vs deflection curve for hº with 25 kg/m$^3$ of fibers. Stirrups Φ6.

**Figura 15.** Load vs. deflection curve for Hº with 25 kg/m$^3$ of fibers. Stirrups Φ10.
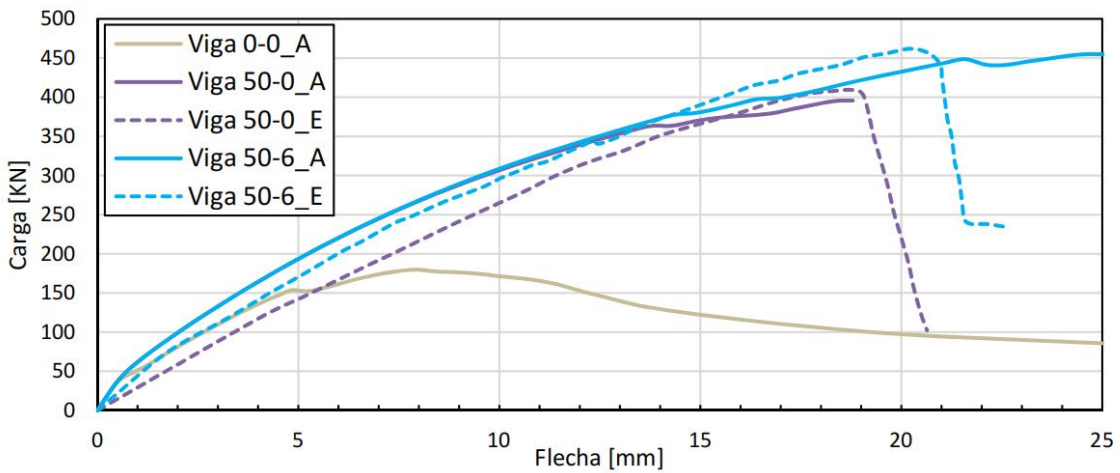


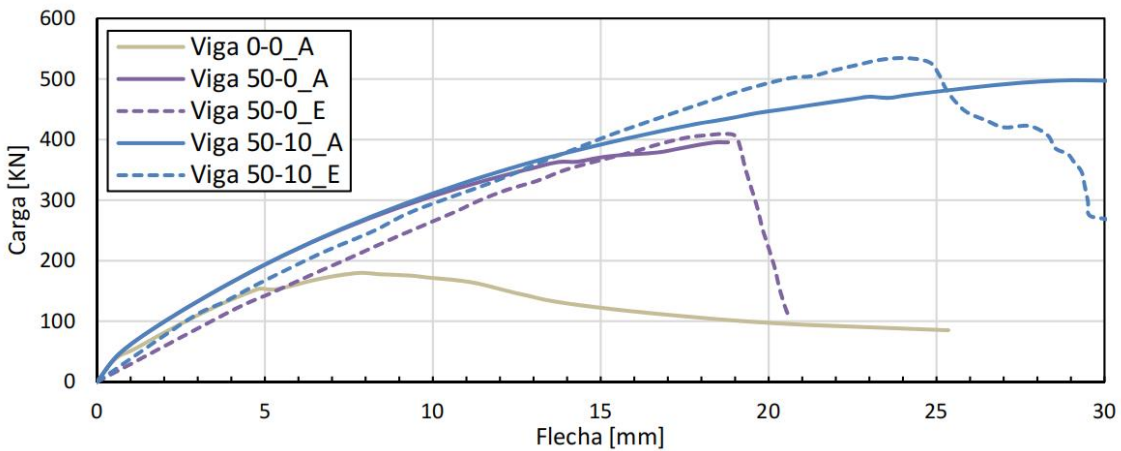**Figure 16.** Load vs deflection curve for º with 50 kg/m$^3$ of fibers. Stirrups Φ6.



**Figure 17.** Load vs deflection curve for Hº with 50 kg/m$^3$ of fibers. Stirrups Φ10.

Figures 18 and 19 show, qualitatively, the location of cracks by means of equivalent plastic deformation maps. In Figure 18, the characteristic shear failure for a reinforced concrete beam is observed, and as expected, the addition of fibers generates, due to their stitching action together with the stirrups, a multiple cracking pattern and a reduction of the crack widths, forming a more diffuse pattern (Figure 19). This results in a better stress transfer, reducing the damage to the support zone.
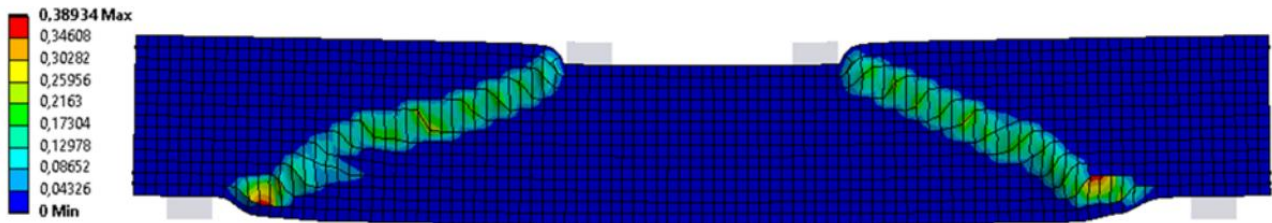
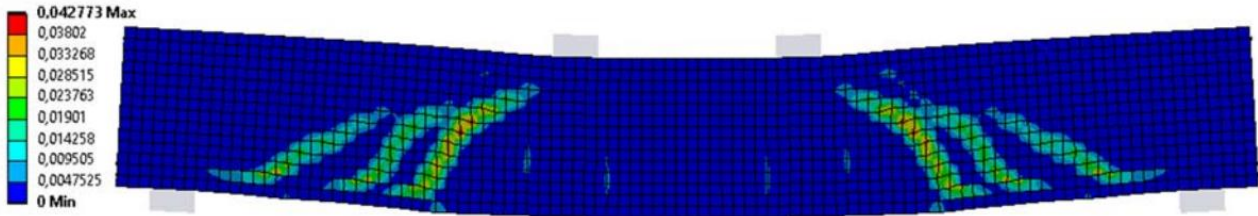**Figure 18.** Equivalent plastic deformation map for Beam 0-6_A. Deformation x5.



**Figure 19.** Equivalent plastic deformation map for beam 25-6_A. Deformation x5.

## 5. Conclusions

Based on the results obtained from the numerical reproduction of the FIP shear test behavior, it can be said that: (1) The numerical model is able to reproduce the behavior at material level during shear failure. (2) Although it is known that the energy (area under the load-failure curve in bending tests) increases with fiber content (Table 3), the response in the FIP shear test is not sensitive to energy for values greater than 400 N/m. (3) Table 3 shows that as the fiber content increases, parameters such as $\Omega_{cr}$ must be increased in order to satisfactorily adjust the experimental response. This parameter is associated with the crushing energy, and it is logical to assume that it increases as the fiber content increases.

Based on the results obtained from the numerical simulation of the behavior and shear failure of HARF beams, it can be said that: (1) Strength increases with fiber content, stirrup incorporation and stirrup diameter, but the effect of the fibers is more important than that of the transverse reinforcement. (2) As the fiber content increases, the stresses in the transverse reinforcement decrease. (3) Increasing the fiber content results in failure with equivalent plastic deformations that are more dispersed in the beam. This is consistent with the stitching effect produced by the steel fibers in the concrete, preventing the formation of large cracks and leading to a more distributed cracking pattern in the failure zone. (4) The incorporation of fibers contributes to the transfer of stresses to the longitudinal reinforcement and can change the type of brittle shear failure to a ductile flexural failure mechanism.

### Collaborators

Facundo Isla Calderón and Bibiana Luccioni (Instituto de Estructuras, Universidad Nacional de Tucumán and Conicet).

### Conflicts of Interest

The author declares no conflicts of interest regarding the publication of this paper.

## References

[1] Möller, O. 2007. Hormigón Armado - Conceptos básicos y diseño de elementos con aplicación.

[2] Fasciolo, M., Conforti, A., Zerbino, R., & Plizzari, G. 2018. Control de fisuración en vigas de hormigones reforzados con diferentes fibras. HAC2018 Congreso Iberoamericano de Hormigón Autocompactante y Hormigones Especiales, 619-628.

[3] Zerbino, R., Barragán, B. E., Conforti, A., Cuenca Asensio, E., Gettu, R., Giaccio, G. Vivas, J. C. 2020. Hormigón Reforzadon con Fibras. Asociación Argentina de Tecnología del Hormigón (AATH).

[4] Amin, A. 2015. Post Cracking Behaviour of Steel Fibre Reinforced Concrete: from Material to Structure. Tesis doctoral.

[5] di Prisco, M; Colombo, M; Dozio, D. 2013. Fibre-reinforced concrete in fib Model Code 2010: principles, models and test validation. *Structural Concrete*, 14: 342-361.

[6] Código Modelo fib 2010. 2012. Final draft. fib CEB-FIP bulletin 65-66. Fédération Internationale du Béton, Switzerland.

[7] Amin, A; Foster, S;. 2016. Shear strength of steel fibre reinforced concrete beams with stirrups. *Engineering Structures*, 323-332.

[8] Menetrey, P., & Willam, K. 1995. Triaxial failure criterion for concrete and its generalization. *ACI Structural Journal*, 92: 311-318.

[9] Frediani, M; Almenar, M; Luccioni, B. 2019. Refuerzo de vigas de hormigón armado con hormigón de altas prestaciones reforzado con fibras. Proyecto Final de Carrera de Ingeniería Civil.

[10] Khanlou, A; MacRae, G; Scott, A; Hicks, S; Clifton, G. 2013. Shear Performance of Steel Fibre-Reinforced Concrete. Steel Innovatios Conference.